Journal of Physics D:
Applied Physics

PURPOSE-LED
PUBLISHING™

PAPER • OPEN ACCESS

Ultrathin tungsten films enabling enhanced electrical response to spin currents

To cite this article: José Ignacio Morales-Aragonés *et al* 2026 *J. Phys. D: Appl. Phys.* **59** 175301

View the article online for updates and enhancements.

You may also like

- Interpolation-based data augmentation for film thickness regression in atmospheric pressure plasma jet deposition via optical emission spectroscopy
Jia-He Tee, Mao-Chuan Chen, Wei-Chuan Hong et al.

- Structural evolution, charge transport, hopping conduction, and electrochemical response of Co^{2+} substituted spinel ferrites
Jyothi A Goudar, Thrinethra S N, Sharanappa Chapi et al.

- Machine learning-aided modeling and absorption optimization in stacked-absorber heterojunction solar cells
Kazi Abrar Shafin, Md Alamin Hossain Pappu, Ahnaf Tahmid Abir et al.

This content was downloaded from IP address 155.210.44.31 on 04/05/2026 at 11:04

IOP Publishing J. Phys. D: Appl. Phys. **59** (2026) 175301 https://doi.org/10.1088/1361-6463/ae5dde

Journal of Physics D: Applied Physics

OPEN ACCESS

RECEIVED
13 January 2026

REVISED
1 April 2026

ACCEPTED FOR PUBLICATION
10 April 2026

PUBLISHED
27 April 2026

Original content from this work may be used under the terms of the Creative Commons Attribution 4.0 licence.

Any further distribution of this work must maintain attribution to the author(s) and the title of the work, journal citation and DOI.

PAPER

Ultrathin tungsten films enabling enhanced electrical response to spin currents

José Ignacio Morales-Aragonés[1], **Inge Groen**[2], **Luis E Hueso**[2,3], **Fèlix Casanova**[2,3], **José Ángel Pardo**[1,4,5], **Carlos Sánchez-Azqueta**[6], **José María De Teresa**[1,7,*] and **Soraya Sangiao**[1,4,7,*]

[1] Instituto de Nanociencia y Materiales de Aragón (INMA), CSIC-Universidad de Zaragoza, 50009 Zaragoza, Spain
[2] CIC nanoGUNE BRTA, Donostia-San Sebastián 20018, Basque Country, Spain
[3] IKERBASQUE, Basque Foundation for Science, 48009 Bilbao, Basque Country, Spain
[4] Laboratorio de Microscopías Avanzadas (LMA), Universidad de Zaragoza, 50018 Zaragoza, Spain
[5] Departamento de Ciencia y Tecnología de Materiales y Fluidos, Universidad de Zaragoza, 50018 Zaragoza, Spain
[6] Departamento de Física Aplicada, Universidad de Zaragoza, 50009 Zaragoza, Spain
[7] Departamento de Física de la Materia Condensada, Universidad de Zaragoza, 50009, Zaragoza, Spain
[*] Authors to whom any correspondence should be addressed.

E-mail: deteresa@unizar.es and sangiao@unizar.es

Keywords: spintronics, ultrathin tungsten films, inverse spin Hall effect, spin pumping, spin Hall conductivity, spin-charge conversion

Abstract

The efficient detection of spin currents is crucial for the development of next-generation spintronic devices. Here, we demonstrate that ultrathin W layers, with thicknesses down to 2 nm—equivalent to only four atomic planes—allow for highly efficient spin-to-charge conversion. From spin pumping experiments in YIG/W bilayers, we analyzed the inverse spin Hall effect (SHE) voltage dependence on W thickness and extracted a spin Hall conductivity of $\sigma_{SH} = -1.14\,(6) \times 10^5\ \Omega^{-1}\ m^{-1}$, yielding effective spin Hall angles ranging from $-0.27\,(4)$ to $-0.88\,(4)$ over the investigated thickness range. Furthermore, assuming the Elliott–Yafet spin scattering mechanism dominates, we estimate a spin diffusion length $\lambda_{sd} = 4.3\,(5) \times 10^{-15}\Omega m^2/\rho_W$, where the W resistivity ρ_W is strongly dependent on thickness. Structural characterization, together with room-temperature electrical resistivity measurements and the high spin-to-charge conversion efficiency observed, confirms the stabilization of the β-phase in these ultrathin W layers. We demonstrate that the monotonic increase of the inverse SHE voltage with decreasing W thickness persists down to 2-nm-thick W layer, reflecting the extremely short spin diffusion length. This allows for efficient spin-current detection in W layers below 5 nm, effectively doubling the voltage output at half the thickness. In the thinnest sample, a continuous 2-nm-thick W layer, the generated voltage exceeds 0.5 mV—well within the operating range of conventional electronics. These findings demonstrate not only the feasibility of spin-current detection in ultrathin W, but also its compatibility with conventional electronics. They highlight the strong potential of integrating ultrathin W layers with high-quality YIG films for the development of energy-efficient spintronic devices and sensors.

1. Introduction

Spintronics is a technology that exploits the intrinsic spin of electrons, in addition to their charge, to store, manipulate, and transmit information. It aims to drastically reduce power consumption in the next generation of integrated processing circuits and to enable faster switching speeds. Spin currents can be nearly dissipationless, and future spintronic logic devices may lead to significant reductions in power consumption and the development of more efficient processors [1–7]. However, since some peripheral and human interface devices still rely on conventional charge-based electronics, efficient conversion between spin and charge currents remains a key challenge for advancing spintronic technologies.

The spin Hall effect (SHE) [8] and its inverse (ISHE) [9] are widely employed to interconvert charge and spin currents. Both phenomena arise from spin–orbit coupling (SOC) within a material: the SHE converts a longitudinal charge current into a transverse pure spin current, whereas the ISHE performs

© 2026 The Author(s). Published by IOP Publishing Ltd

the inverse process. The efficiency of spin-to-charge conversion is a crucial figure of merit in spintronic systems, as it directly affects the ability to transduce spin currents into detectable charge signals [10, 11]. Metals such as Al [12], Ta [13, 14], Pt [13, 15–18], Mo [13, 15], Nb [13], Au [15, 19–21], Pd [15, 22] and the semimetal Bi [23–25] have been extensively studied for spin-to-charge conversion due to their varying degrees of SOC. Tungsten (W), in particular, exhibits strong SOC owing to its high atomic number, making it highly effective at converting spin current into charge signals via ISHE. The spin-to-charge conversion efficiency in W layers is highly sensitive to crystal structure, and the quality of the interface with the ferromagnetic layer also plays a significant role [26]. Thus, W is an outstanding spin–orbit material, and a detailed understanding of its spin transport properties is essential for reducing energy consumption in memory and spintronic logic devices, as well as for enhancing signal readout in spin-based sensors [27].

In this work, we investigate spin-to-charge conversion via ISHE in thin and ultrathin W films focusing on previously unexplored behavior below 5 nm and leveraging the strong SOC characteristic of the β-phase, as reported in earlier studies [28, 29]. Spin currents are generated using the spin pumping technique [30], in which ferromagnetic resonance (FMR) is excited in a magnetic layer, resulting in the injection of a pure spin current into an adjacent W layer. $Y_3Fe_5O_{12}$ (YIG) is employed as the magnetic layer due to its combination of low dielectric losses, very narrow FMR linewidth associated with low Gilbert damping, and electrical insulating properties, which suppress spurious charge currents and related unwanted effects [31]. To evaluate the spin-to-charge conversion efficiency in W layers, we systematically investigated the dependence of the ISHE signal in YIG/W bilayers on several parameters, with particular emphasis on W thickness, achieving continuous and uniform W layers as thin as 2 nm. This analysis also enabled the extraction of the spin diffusion length and spin Hall angle of W and has allowed us to correlate these parameters with the structural characteristics of the W layers, as determined by x-ray diffraction (XRD) and high-resolution transmission electron microscopy (HRTEM).

2. Methods

To evaluate the spin-to-charge conversion efficiency, six samples were fabricated: five YIG/W bilayers with nominal W thicknesses of 2, 4, 8, 10, and 12 nm, and one reference sample without a W layer for the initial magnetic characterization of the YIG film. The samples were prepared from a commercial 300 nm-thick YIG films provided by Innovent e.V. (Jena, Germany). YIG was grown by liquid phase epitaxy on a (111) gadolinium gallium garnet ($Gd_3Ga_5O_{12}$, GGG) substrate and cut in pieces measuring 5×2.5 mm^2. Subsequently, W layers of the specified nominal thicknesses (2–12 nm) were deposited onto the YIG layer via magnetron sputtering using an Ar pressure of 3 mTorr, a deposition rate of 0.11 Å s^{-1}, an applied power of 10 W and a base pressure of 2×10^{-8} Torr at room temperature. To prevent oxidation, a 5 nm-thick SiO_2 capping layer was subsequently deposited on the W layers via magnetron sputtering at an Ar pressure of 3 mTorr, an applied power of 200 W and a deposition rate of 0.5 Å s^{-1}. For each W thickness, a representative sample was fabricated and measured, with all depositions performed in the same sputtering campaign under identical conditions to minimize batch variability.

The samples were characterized using a broadband spin pumping system based on a custom microantenna/holder setup, schematically shown in figure 1. The microantenna consists of a centrally shorted microstrip line, flanked by two copper strips for voltage measurements. The microstrip line receives a radio-frequency (RF) signal from an external Keysight N5173B signal generator, while the lateral strips are connected via a twisted-pair cable to a Stanford Research Systems SR830 lock-in amplifier.

Each sample was mounted face-down onto the microantenna, with its edges electrically connected to the lateral copper strips using silver paint. The entire assembly was positioned between the poles of an adjustable electromagnet, with the static magnetic field oriented along the microstrip direction. In this configuration, the RF magnetic field generated by the microantenna is oriented perpendicular to the static field, thereby optimally exciting FMR in the YIG layer and enabling the injection of a pure spin current into the W layer via spin pumping.

The voltage generated at the sample edges, arising from spin-to-charge current conversion, was measured with an SR830 lock-in amplifier operating at a few kHz, matching the frequency of the square-wave modulation applied to the RF excitation.

FMR detection in the YIG layer was carried out by monitoring the power reflected from the microantenna. The onset of FMR is evidenced by a distinct negative peak in the reflected power signal. To separate the incident RF wave generated by the source from the wave reflected from the microantenna, a three-port magnetic circulator was employed. This circulator, connected to the RF generator

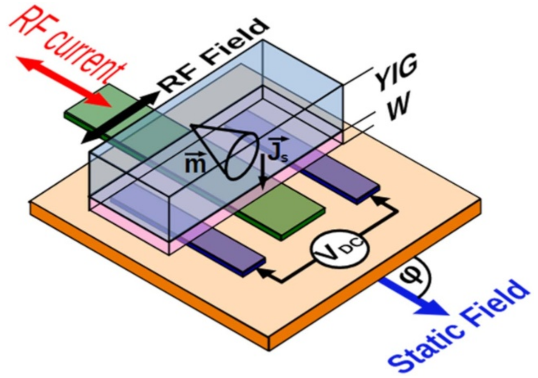

Figure 1. Schematic of the experimental setup for ISHE voltage measurements, showing the microstrip line driving the RF current, the associated RF magnetic field, the static magnetic field, the voltage measurement strips and the sample on top with the W layer facing downward.

output, redirected the reflected signal toward an RF power meter, enabling the characteristic FMR signature to be identified from the meter's response.

For structural characterization, the samples were analyzed using HRTEM and scanning transmission electron microscopy (STEM). STEM images were obtained using a *FEI Titan Analytic* scanning transmission STEM electron microscope with high resolution HRTEM capabilities. XRD profiles were measured with a PANalytical Empyrean multipurpose diffractometer, while x-ray reflectivity (XRR) profiles were acquired with a Bruker D8 Advance high-resolution diffractometer and analyzed using LEPTOS software (Bruker AXS).

Electrical characterization of the YIG/W bilayers was performed at room temperature using a Cascade Microtech M150 microprobe station.

3. Results

3.1. Structural characterization

The thicknesses of the W layers and the roughness of the YIG/W interfaces were obtained by fitting the experimental XRR profiles and are as follows: 1.9(3), 3.7(4), 7.6(4), 9.2(4), and 11.4(4) nm; these are the values used in all fits or analysis in which the W-layer thickness appears in this work. However, for clarity, the nominal values of 2, 4, 8, 10 and 12 nm—very close to the experimentally determined ones—are used throughout the paper. The roughness of the YIG/W interface, extracted from the XRR fits, was found to be in the range of 0.3–0.5 nm for all samples. This relatively low roughness suggests high transparency for pure spin current injection, consistent with the comparatively large spin-mixing conductance extracted for these interfaces.

For HRTEM observations, electron-transparent lamellae were prepared from the YIG/W bilayers using a combined focused ion beam-scanning electron microscope dual beam system. Representative cross-sectional micrographs of the thickest and thinnest samples are presented in figure 2. HRTEM analysis confirms the monocrystalline nature of the YIG layer and reveals a preferential growth orientation in the W films. Crystalline W grains, typically several tens of nanometers in lateral size, are predominantly aligned along the in-plane direction of the YIG layer. The roughness at both the YIG/W interface and the free surface of the W layers is below 0.5 nm, in agreement with the XRR results.

W is known to crystallize in two distinct phases, α and β, which exhibit markedly different physical properties. To determine the crystalline phase present in our W films, XRD measurements were performed. The XRD pattern of the 12 nm-thick W sample, shown in figure 3, exhibits relatively low signal intensity and considerable noise, even for the thickest W layer, likely due to the small scattering volume and the polycrystalline nature of the films. Nonetheless, characteristic diffraction peaks corresponding to β-W are clearly visible. One of these peaks nearly overlaps with a reflection common to both α- and β-W; therefore, it has been labeled accordingly in figure 3. These results confirm the stabilization of the β-phase in the W layers of our samples. Although the signal-to-noise ration in the XRD pattern is limited by the small film thickness, the diffraction peak positions are fully consistent with β-W, and no additional reflections characteristic of α-W are detected. This conclusion is further supported by previous reports showing that W layers thinner than 20 nm—significantly thicker than any of those studied

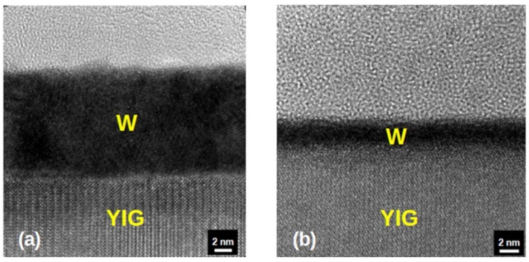

Figure 2. Cross-sectional HRTEM micrographs of a YIG/W stack with a W layer of: 12 nm in thickness (a) and 2 nm in thickness (b).

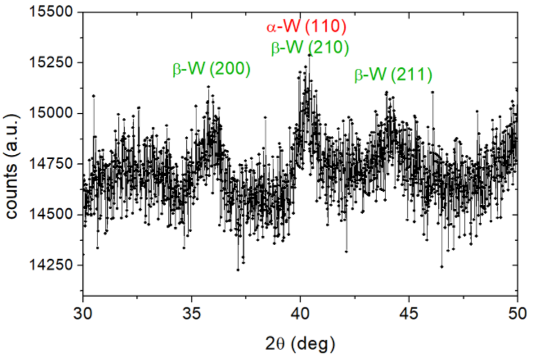

Figure 3. XRD pattern for the GGG//YIG/W(12 nm) sample.

here—tend to stabilize in the β-phase [32]. Additional confirmation comes from prior measurements on lateral spin valves employing sputtered W, prepared by the same research group that provided the W layers for this study under identical growth conditions, which also indicated the presence of the β-phase [27].

3.2. Room-temperature charge transport characterization

Previously reported room-temperature electrical resistivity values for W show a strong phase dependence: approximately 25 $\mu\Omega$ cm for the α-phase and about 200 $\mu\Omega$ cm for the β-phase [32]. The spin Hall angle also exhibits strong phase dependence: β-W has reported values between -0.3 and -0.5 [28, 33, 34], while α-W generally displays absolute values below 0.07 [28, 35]. Electrical resistance measurements conducted on our samples, in combination with the geometrical dimensions of the layers, allowed us to calculate their resistivities. For thin films, surface scattering effects make resistivity thickness dependent, and the measured values can be fitted to the Fuchs–Sondheimer model [36, 37]. This fitting, shown in figure 4, yields a bulk resistivity of 207 $\mu\Omega$ cm, very close to the value reported for β-W phase in the literature of 195 $\mu\Omega$ cm [32].

The dependence of W resistivity on layer thickness, $\rho_W(t_W)$, was determined by fitting their experimental values to the theoretical Fuchs–Sondheimer model, which accounts for surface scattering effects on conduction electrons in the ultrathin limit [36, 37]. Figure 4 shows the resistivity values obtained for each sample as a function of W-layer thickness, with the solid red line representing the fit to the Fuchs–Sondheimer model:

$$\rho_W = \frac{\rho_0}{1 - \frac{3}{8}\frac{l_0}{t_W}}$$

with $\rho_0 = 207\ \mu\Omega\ cm$ the bulk resistivity and $l_0 = 3.7\ nm$ the mean free path of conduction electrons in W. This yields the experimental dependence of W resistivity on layer thickness $\rho_W(t_W)$, which will be used in the analysis of the ISHE voltage in YIG/W bilayers as a function of W thickness in the following subsection.mOhm

3.3. FMR-based spin pumping characterization

FMR measurements were initially carried out on the 300 nm-thick YIG film deposited on a GGG substrate, prior to W layer deposition. At each measured frequency, the FMR inductive signal was acquired,

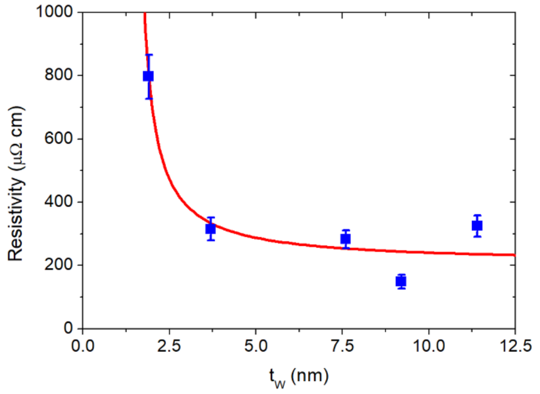

Figure 4. Resistivity as a function of the thickness of the W layer. Solid line corresponds to the fitting to the Fuchs–Sondheimer model.

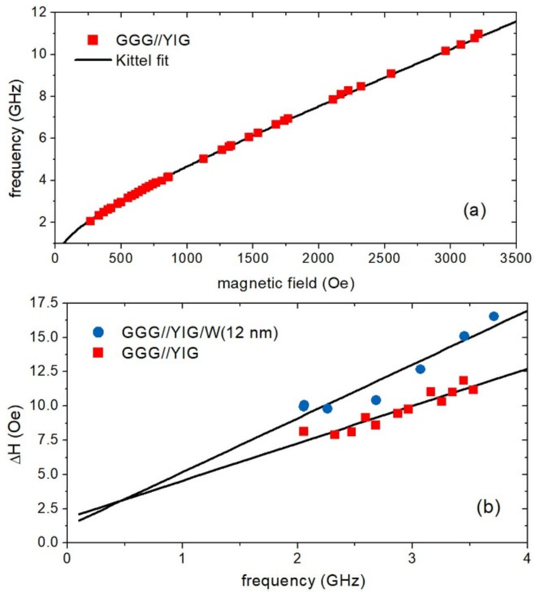

Figure 5. (a) Resonance frequency as a function of resonance magnetic field for a GGG//YIG(300 nm) thin film. Solid line corresponds to the fitting to Kittel equation. (b): Full FMR linewidth versus resonance frequency for the YIG layer with (blue dots) and without (red squares) the adjacent W. Solid lines correspond to the fit to a linear dependence.

and the resonance field (peak center) and linewidth were determined from the signal analysis. Fitting the resonance field as a function of frequency to the Kittel equation $\omega = \gamma\sqrt{H_0\left(H_0 + 4\pi M_S\right)}$ (see figure 5(a)) allowed extraction of the saturation magnetization and gyromagnetic ratio, resulting in values of $M_{S\_YIG} = 160.9\ \frac{emu}{cm^3}$ and $\gamma_{YIG} = 1.67 \times 10^{11}\ \frac{rad}{s\ T}$ respectively. Both values are in close agreement with those reported for bulk YIG in [38]. The Gilbert damping parameter α_{YIG} was determined from the linear fit of the linewidth as a function of frequency [39] (red triangles in 5(b)), resulting in a value of $\alpha_{YIG} = 3.62 \times 10^{-3}$. These values are consistent with those previously reported for YIG thin films of similar thickness [23, 39–42].

FMR excitation in the YIG layer induces spin pumping in the adjacent W layer, resulting in the injection of a pure spin current into the W layer. This additional spin-current dissipation mechanism leads to an enhanced effective damping in the YIG layer. The increased slope observed in the linear dependence of the linewidth on frequency, as shown by the blue dots in figure 5(b), indicates an increased damping and provides insight into the spin transfer efficiency across the YIG/W interface.

Measurements on the sample with the thickest W layer (12 nm), which ensures full spin current absorption without reflection, yielded an enhanced Gilbert damping parameter of $\alpha_{YIG/W} = 5.21 \times 10^{-3}$. The linewidth showed no significant dependence of W thickness at a fixed frequency, indicating complete absorption of the spin current even in the 2 nm W layer and a spin diffusion length shorter than

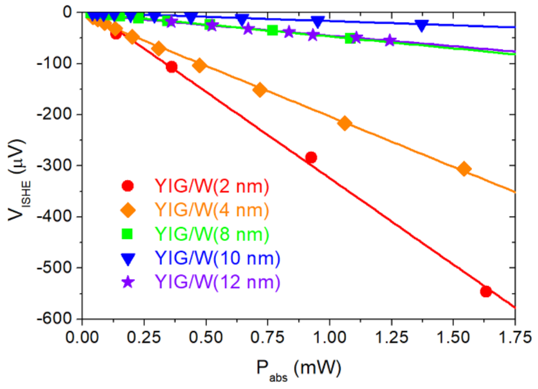

Figure 6. Dependence of the ISHE voltage peak height at 2.055 GHz on the power absorbed via FMR in YIG/W stacks for all investigated W layer thicknesses.

the thinnest layer studied. In the microstrip geometry used here, the dominant excited mode corresponds to the uniform FMR mode, as confirmed by the Kittel dispersion and the absence of higher-order spin-wave resonances. Since both α_{YIG} and $\alpha_{YIG/W}$ are extracted from the same resonance branch under identical conditions, the relative damping enhancement reliably reflects interfacial spin pumping.

The difference in damping between the YIG/W bilayers and bare YIG samples allows for the calculation of the effective spin-mixing conductance, which characterizes the efficiency of spin transfer across the YIG/W interface [23]:

$$g_{\uparrow\downarrow\, eff} = \left(\alpha_{YIG/W} - \alpha_{YIG}\right) \frac{4\pi M_{s\_YIG} t_{YIG}}{g\,\mu_B} = 4.15 \times 10^{18}\ m^{-2}$$

where t_{YIG} is the YIG layer thickness, g is the Landé factor, and μ_B is the Bohr magneton.

This value is approximately four times greater than the one reported in [43] for the YIG/W interface, but very similar to the value the same authors reported previously for the same interface in their topical review [44]. It should be noted, however, that effective spin-mixing conductance in YIG/heavy metal systems is highly sensitive to interface preparation, growth conditions, and fitting procedures, and values spanning more than one order of magnitude are commonly reported in the literature; therefore, a factor-of-four variation remains within the typical experimental dispersion. The obtained spin-mixing conductance leads to a corresponding spin-mixing conductivity of:

$$G_{\uparrow\downarrow\, eff} = \frac{e^2}{h} g_{\uparrow\downarrow eff} = 1.61 \times 10^{14}\ \boldsymbol{\Omega}^{-1} m^{-2}.$$

After interface characterization, measurements of the ISHE voltage (V_{ISHE}) were carried out. The V_{ISHE} peak height was analyzed as a function of the power absorbed via FMR, with results for an excitation frequency of 2.055 GHz presented in figure 6. A pronounced linear relationship was found across all W layer thicknesses, in agreement with earlier studies [15, 45, 46]. This indicates that the measurements were conducted within the linear response regime, enabling all V_{ISHE} values to be normalized to a common reference absorbed power. Due to the pronounced frequency- and sample-dependent variations in the FMR-delivered power in our shorted microstrip setup, such normalization is crucial for an accurate comparison of the V_{ISHE} for different W layer thicknesses.

Considering the V_{ISHE} measurements performed on all YIG/W bilayers with varying W thicknesses, we normalized the data to a common FMR absorbed power and fitted the peaks to Lorentzian profiles, extracting the V_{ISHE} peak height as a function of W thickness. This is shown in figure 7 for the voltage peaks measured at 2.055 GHz.

A maximum absolute voltage peak height exceeding 500 μV was recorded for the GGG//YIG/W (2 nm) sample at 2.055 GHz. A monotonic decrease of V_{ISHE} with increasing W thickness was observed for thicknesses below 10 nm, consistent with the spin-diffusion equation with the appropriate experimental boundary conditions [45, 47]:

$$V_{ISHE} = \theta_{SH} \frac{hLP\,f\,sin^2\left(\phi\right)}{2e\,t_W} \frac{G_{\uparrow\downarrow}}{G_{\uparrow\downarrow} + \frac{1}{\rho_W(t_W)\lambda_{sd}} \frac{1-exp\left(\frac{-2t_W}{\lambda_{sd}}\right)}{1+exp\left(\frac{-2t_W}{\lambda_{sd}}\right)}} \frac{\left(1-exp\left(\frac{-t_W}{\lambda_{sd}}\right)\right)^2}{1+exp\left(\frac{-2t_W}{\lambda_{sd}}\right)} \tag{1}$$

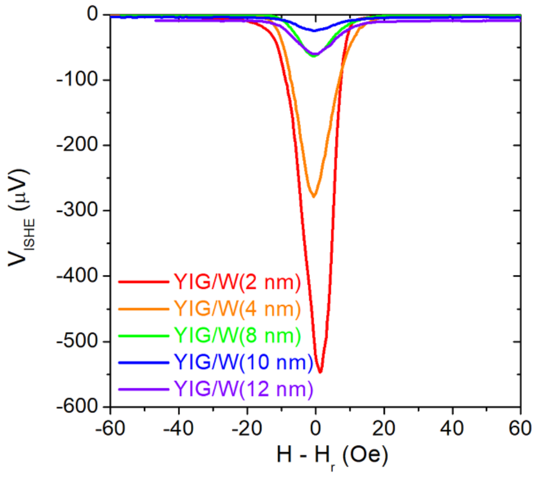

Figure 7. V_{ISHE} peak height as a function of the static magnetic field for different thicknesses of the W layer at 2.055 GHz for a power absorbed by the FMR within the YIG layer of 1.6 mW.

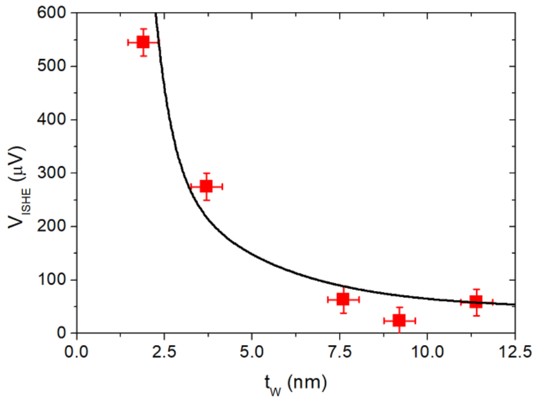

Figure 8. ISHE voltage as a function thickness of the W layer at 2.055 GHz. Black solid line corresponds to the fitting to expression (1).

Here θ_{SH} is the spin Hall angle, characterizing the efficiency of the spin-to-charge conversion in the W layer, λ_{sd} is the spin diffusion length in W, which characterizes the decay of the injected spin current, L is the length of the YIG/W stack being excited at a frequency f by the microwave signal, corresponding to the microstrip line width, ϕ is the angle of magnetization precession in the YIG layer, P is the ellipticity correction factor [48], t_W is the thickness of the W layer, and $\rho_W(t_W)$ is its resistivity, which is a function of the thickness of the W layer t_W. The ellipticity P was computed using the analytical expressions provided in [48], while the precession cone angle ϕ was calculated as: $\phi = \frac{h_{RF}}{\Delta H}$ [49], where ΔH is the FMR linewidth and h_{RF} the amplitude of the RF magnetic field, estimated as 0.1 Oe from the geometry and power characteristics of the microstrip line. The corresponding precession cone angle is 0.8°. The RF magnetif field amplitude was obtained from full electromagnetic simulations of the microstrip geometry using the Sonnet EM solver, yielding an RF field of 0.09 Oe at the sample position, consistent with the value used for the cone angle estimate.

The spin Hall angle θ_{SH} can be written in terms of the spin Hall conductivity σ_{SH} and the longitudinal resistivity as $\theta_{SH} = \sigma_{SH}\rho_W$. Furthermore, assuming the Elliott–Yafet spin scattering mechanism dominates spin relaxation, spin diffusion length λ_{sd} also scales linearly with $\frac{1}{\rho_W}$ [50–52]. The experimental data were fitted using this model, with only two free parameters: σ_{SH} and the product $\lambda_{sd}\rho_W$. Figure 8 presents the results of the fitting procedure. The extracted values that best reproduce the experimental data are $\sigma_{SH} = -1.14(6) \times 10^5\ \Omega^{-1}\ m^{-1}$ and $\lambda_{sd}\rho_W = 4.3(5) \times 10^{-15}\Omega\ m^2$.

4. Discussion

The obtained results for both free parameters, σ_{SH} and $\lambda_{sd}\rho_W$, lead to θ_{SH} values ranging from $-0.27\,(4)$ to $-0.88\,(4)$ over the investigated thickness range and λ_{sd} values from 0.5(3) for the 2 nm-thick sample, 1.2(4) for the 4 nm-thick sample and 1.7(4) for thicker samples. These values are in reasonable agreement with values reported in the literature [28, 29, 33, 53–56]. For the 2 nm film, the extracted λ_{sd} value should be regarded as an effective spin diffusion length, as finite-size effects and enhanced surface spin–orbit scattering introduce additional spin relaxation channels that renormalize the apparent value below the bulk β-W range. This behavior is consistent with Elliott–Yafet scaling when thickness approaches the spin relaxation length. Furthermore, we extract an absolute spin Hall angle greater than 0.27(4), which corresponds to a spin-to-charge conversion efficiency in the W layer exceeding 27(4)%. This high value for the spin Hall angle in W is comparable to the values previously reported, which are in the range between -0.22 [54] and -0.50 [33], with numerous studies reporting values within this interval [28, 29, 32, 33, 54–56].

The spin Hall conductivity extracted from our measurements, $\sigma_{SH} = -1.14\,(6) \times 10^5\ \Omega^{-1}\ m^{-1}$, falls well within the range of previously reported values for β-W. Earlier studies report values as low as $-2 \times 10^5\ \Omega^{-1}\ m^{-1}$ [57] and typically around $-10^5\ \Omega^{-1}\ m^{-1}$ [58], indicating that our result is fully consistent with experimental expectations. The experimentally extracted spin Hall conductivity represents an effective spin Hall conductivity that includes both intrinsic and extrinsic scattering contributions. While first-principles calculations predict a dominant intrinsic component in β-W, disentangling microscopic mechanisms would require dedicated disorder or temperature-dependent studies beyond the scope of this work. The monotonic thickness dependence observed here does not indicate an anomalous interface-driven enhancement. Remarkably, the value we have obtained is very close to the intrinsic spin Hall conductivity of β-W predicted by first-principle calculations, $-1.255 \times 10^5\ \Omega^{-1}\ m^{-1}$ [59], highlighting that the ultrathin W layers in our study achieve a spin-to-charge conversion efficiency approaching the theoretical limit. This close agreement not only validates our experimental approach but also underscores the high quality of the W films and emphasizes their potential for applications in high-efficiency spintronic devices.

The minimum extracted spin diffusion length, 0.5(3) nm, is on the lower end compared to previously reported values for W, but its average is within the range of them, which usually lie between 1 and 3 nm [33, 53, 60, 61]. The interplay between spin diffusion length and layer thickness is essential: reducing the W thickness increases its resistivity and enhances the generated ISHE voltage, but, once the film is thinner than the spin diffusion length, the spin current is only partially absorbed and the ISHE-induced charge current decreases. An optimal tradeoff between these two tendencies result in a maximum value of ISHE voltage, typically reached at layer thicknesses comparable to the spin diffusion length [23, 45, 62]. Moreover, because the spin diffusion length itself strongly depends on the resistivity of the material, and thus on the layer thickness, this interplay must be properly accounted for to achieve a realistic modeling of the experiment. This considerations leads to the experimentally obtained relationship $\lambda_{sd} = 4.3\,(5) \times 10^{-15}\ \boldsymbol{\Omega}\ m^2/\rho_W$ [50].

For W, the highest ISHE voltage values prior to the present study were reported for 5 nm-thick layers, showing a monotonic increase of the ISHE voltage with decreasing thickness. Our measurements confirm that this behavior persists below 5 nm, with the maximum ISHE voltage observed in an ultrathin W layer of 2 nm in thickness (corresponding to approximately 4 atomic planes), with an interesting 100% increase in the ISHE voltage peak height compared to the value obtained for the 4 nm-thick layer.

ISHE voltages are commonly measured using lock-in techniques and specialized setups designed to detect extremely small signals, often requiring large spin currents to enhance the response. However, for practical implementations of spin-current detection based on ISHE, it is essential to reach voltage levels compatible with standard electronic circuitry, enabling straightforward integration. Differential voltage inputs offer the highest sensitivity, with minimum detectable voltages on the range from 50 to 100 μV and input impedances typically exceeding 100 kΩ [63]. For effective interfacing with such electronics, the ISHE voltage generated by the high-SOC layer must significantly exceed 100 μV, while its internal impedance should remain well below the input impedance. This voltage range must be achieved considering moderate spin-current intensities, suitable for integration into practical future devices.

For a meaningful comparison of bilayer efficiencies, the ISHE voltage should be expressed per unit length, that is, the induced electric field, since the measured voltage scales with the sample length under FMR excitation. The intensity of the injected spin current must also be normalized, which can be quantified through the square of the precession cone angle in FMR or, equivalently, through the square of the RF field used to drive the FMR. Our measurements yield a precession cone angle of approximately 0.8°,

Table 1. Comparison of the highest ISHE electric-field values reported in the literature, normalized to our experimental conditions.

V_{ISHE} (μV)	Bilayer	Length excited by FMR (mm)	RF field (Oe)	Normalized electric field (μV mm^{-1})	References
5260	YIG/W (20 nm)/(5 nm)	5	0.3	**117**	Wang *et al* [64]
1000	YIG/Pt (20 nm)/(5 nm)	5	0.3	**22**	Du *et al* [65]
2000	YIG/W (20 nm)/(5 nm)	5	0.3	**44**	Du *et al* [43]
5100	YIG/Ta (20 nm)/(5 nm)	5	0.3	**113**	Wang *et al* [66]
450	Py/Pt (15 nm)/(15 nm)	2.92	4.5	**16**	Mosendz *et al* [68]
540	YIG/W (300 nm)/(2 nm)	1	0.1	**540**	This work

corresponding to an RF field of about 0.1 Oe, determined by the injected spin-current amplitude. The highest values of ISHE voltage previously reported in literature correspond to Pt, Ta and W layers [43, 64–66], that exhibit also the highest spin Hall angles: 0.12 for Pt [67], and 0.50 for W [33]. The measurements in [43, 64–66] were conducted using spin pumping in a cavity with an RF power of 200 mW and 5 mm-long samples. In this configuration, the entire ferromagnetic volume is irradiated with an RF field of approximately 0.3 Oe [64]. By contrast, in our experiments employing a microstrip antenna for spin pumping, the RF field is reduced by about a factor of 3 (0.1 Oe), and only the region corresponding to the microstrip width (1 mm) is excited. Because the spin-current amplitude scales with the square of the RF field, and the ISHE voltage increases linearly with the sample length under FMR excitation, the ISHE voltages obtained in our experiment are proportionally reduced by these factors compared to previously reported results. Table 1 presents a comparison of the highest ISHE electric-field values reported in the literature, normalized to our experimental conditions (RF field, $h_{\mathrm{RF}} = 0.1$ Oe and an effective sample length of 1 mm under FMR excitation). We emphasize that table 1 provides an order-of-magnitude comparison rather than a strict quantitative benchmarking, as reported ISHE voltages depend sensitively on YIG and interface quality, excitation geometry and detection scheme. Possible orbital Hall contributions, if present, are effectively incorporated into the extracted spin Hall angle. Thermal artifacts are minimized in our microstrip geometry, and the observed symmetry and power dependence of the signal are fully consistent with spin pumping.

In our experiments, the internal impedance of the sample containing a 2 nm-thick W layer is simply its resistance (6.5 kΩ), well below the input impedance of conventional electronic circuitry, and the measured voltage far exceeds the required thresholds for a moderate spin-current intensity corresponding to a precession cone angle of 0.8°. Because these voltage levels surpass the threshold required for interfacing with standard electronics, our results represent not only a substantial improvement in output signal, but also a real opportunity for integration into spin-based sensors and future spintronic logic devices.

5. Conclusions

In summary, we have optimized GGG//YIG/W stacks and determined, from measurements of the ISHE voltage signal in spin pumping experiments, the spin Hall conductivity $\sigma_{SH} = -1.14\,(6) \times 10^5\ \Omega^{-1}\ m^{-1}$ and the product $\lambda_{sd}\rho_W = 4.3\,(5) \times 10^{-15} \Omega\ m^2$. The spin Hall conductivity obtained for β-W in our study is fully consistent with experimental expectations and very close to the intrinsic spin Hall conductivity of β-W predicted by first-principle calculations [59], highlighting that the ultrathin W layers in our study achieve a spin-to-charge conversion efficiency approaching the theoretical limit.

The estimated spin Hall conductivity and the product $\lambda_{sd}\rho_W$ yield spin Hall values ranging from $-0.27\,(4)$ to $-0.88\,(4)$ over the investigated thickness range and λ_{sd} values from 0.5(3) for the 2 nm-thick sample, 1.2(4) for the 4 nm-thick sample and 1.7(4) for thicker samples. These values are in reasonable agreement with values reported in the literature [28, 29, 33, 53–56]. Structural analysis using XRD and HRTEM has confirmed the presence of the crystalline β-phase in the thickest W layer forming the YIG/W stacks. This finding is further supported by the resistivity and the spin Hall angle values obtained in our study. Additional confirmation comes from previous measurements on lateral spin valves made with sputtered W layers prepared by the same research group that provided the W layers for the present study [27].

Remarkably, the successful growth of a uniform and continuous 2 nm-thick W layer has demonstrated the monotonic increase of ISHE voltage with decreasing thickness down to 2 nm, nearly doubling the voltage value observed for the 4 nm-thick layer. The combination of a large spin Hall angle, high resistivity, and short spin diffusion length maximizes spin-to-charge conversion in this ultrathin W layer, enabling it to operate as a voltage generator exceeding 0.5 mV with an internal impedance of 6.5 kΩ.

Therefore, this YIG/W(2 nm) bilayer represents a promising candidate for interfacing future spintronic devices with conventional electronics and underscores the strong potential of integrating ultrathin W layers with high-quality YIG films for the development of advanced energy-efficient spintronic devices and sensors. Practical implementation would require assessment of long-term stability, large-area reproducibility, and process integration. Notably, sputtered tungsten is already widely employed in CMOS-compatible fabrication lines, suggesting favorable prospects for technological scalability. Dedicated reliability and integration studies constitute an important direction for future work.

Acknowledgments

The authors would like to thank the Laboratory for Advanced Microscopies (LMA) and the Institute of Nanoscience and Materials of Aragón (INMA), from CSIC–Universidad de Zaragoza, for providing access to their instruments and expertise.

The authors acknowledge Grants PID2020-112914RB-I00, PID2021-122511OB-I00, PID2023-146451OB-I00, PID2023-150244OB-I00 and PID2024-155708OB-I00, funded by MICIU/AEI/10.13039/501100011033 and ERDF/EU and Grants E13_23R, PROY_E29_24 and PROY_T33_24 funded by Gobierno de Aragón. We warmly acknowledge the help of F. Cazaña and G. Antorrena with the XRD characterization, of I. Rivas with lamellae preparation for TEM observation and of R. Fernández-Pacheco with the TEM characterization.

Author contributions

José Ignacio Morales-Aragonés 0000-0002-9163-9357
Conceptualization (equal), Data curation (equal), Formal analysis (equal), Investigation (equal), Methodology (equal), Software (equal), Writing – original draft (equal)

Inge Groen 0000-0003-2933-033X
Investigation (equal), Methodology (equal), Resources (equal)

Luis E Hueso 0000-0002-7918-8047
Conceptualization (equal), Funding acquisition (equal), Investigation (equal), Methodology (equal), Resources (equal), Writing – review & editing (equal)

Fèlix Casanova 0000-0003-0316-2163
Conceptualization (equal), Funding acquisition (equal), Investigation (equal), Methodology (equal), Resources (equal), Writing – review & editing (equal)

José Ángel Pardo 0000-0002-0111-8284
Investigation (equal), Methodology (equal), Resources (equal)

Carlos Sánchez-Azqueta 0000-0002-8236-825X
Investigation (equal), Methodology (equal), Resources (equal)

José María De Teresa 0000-0001-9566-0738
Conceptualization (equal), Formal analysis (equal), Funding acquisition (equal), Investigation (equal), Methodology (equal), Project administration (equal), Resources (equal), Software (equal), Supervision (equal), Validation (equal), Visualization (equal), Writing – review & editing (equal)

Soraya Sangiao 0000-0002-4123-487X
Conceptualization (equal), Data curation (equal), Formal analysis (equal), Funding acquisition (equal), Investigation (equal), Methodology (equal), Project administration (equal), Resources (equal), Software (equal), Supervision (equal), Validation (equal), Visualization (equal), Writing – original draft (equal), Writing – review & editing (equal)

References

[1] Manipatruni S, Nikonov D E and Young I A 2018 Beyond CMOS computing with spin and polarization *Nat. Phys.* **14** 338–43
[2] Manipatruni S, Nikonov D E, Lin C-C, Gosavi T A, Liu H, Prasad B, Huang Y-L, Bonturim E, Ramesh R and Young I A 2019 Scalable energy-efficient magnetoelectric spin–orbit logic *Nature* **565** 35–42
[3] Ahn E C 2020 2D materials for spintronic devices *npj 2D Mater. Appl.* **4** 17
[4] Barla P, Joshi V K and Bhat S 2021 Spintronic devices: a promising alternative to CMOS devices *J. Comput. Electron.* **20** 805–37

[5] Dieny B *et al* 2020 Opportunities and challenges for spintronics in the microelectronics industry *Nat. Electron.* **3** 446–59
[6] NR 2024 Spintronics for ultra-low-power circuits and systems *Nat. Rev. Electr. Eng.* **1** 691
[7] Fert A, Ramesh R, Garcia V, Casanova F and Bibes M 2024 Electrical control of magnetism by electric field and current-induced torques *Rev. Mod. Phys.* **96** 015005
[8] Sinova J, Valenzuela S O, Wunderlich J, Back C and Jungwirth T 2015 Spin Hall effects *Rev. Mod. Phys.* **87** 1213–60
[9] Saitoh E, Ueda M, Miyajima H and Tatara G 2006 Conversion of spin current into charge current at room temperature: inverse spin-Hall effect *Appl. Phys. Lett.* **88** 182509
[10] Pham V T, Yang H, Choi W Y, Marty A, Groen I, Chuvilin A, Bergeret F S, Hueso L E, Tokatly I V and Casanova F 2021 Large spin-charge interconversion induced by interfacial spin-orbit coupling in a highly conducting all-metallic system *Phys. Rev. B* **104** 184410
[11] Sanz-Fernández C, Pham V T, Sagasta E, Hueso L E, Tokatly I V, Casanova F and Bergeret F S 2020 Quantification of interfacial spin-charge conversion in hybrid devices with a metal/insulator interface *Appl. Phys. Lett.* **117** 142405
[12] Valenzuela S O and Tinkham M 2006 Direct electronic measurement of the spin Hall effect *Nature* **442** 176–9
[13] Morota M, Niimi Y, Ohnishi K, Wei D H, Tanaka T, Kontani H, Kimura T and Otani Y 2011 Indication of intrinsic spin Hall effect in 4d and 5d transition metals *Phys. Rev. B* **83** 174405
[14] Sagasta E, Omori Y, Vélez S, Llopis R, Tollan C, Chuvilin A, Hueso L E, Gradhand M, Otani Y and Casanova F 2018 Unveiling the mechanisms of the spin Hall effect in Ta *Phys. Rev. B* **98** 060410
[15] Mosendz O, Vlaminck V, Pearson J E, Fradin F Y, Bauer G E W, Bader S D and Hoffmann A 2010 Detection and quantification of inverse spin Hall effect from spin pumping in permalloy/normal metal bilayers *Phys. Rev. B* **82** 214403
[16] Liu L, Moriyama T, Ralph D C and Buhrman R A 2011 Spin-torque ferromagnetic resonance induced by the spin Hall effect *Phys. Rev. Lett.* **106** 036601
[17] Azevedo A, Vilela-Leão L H, Rodríguez-Suárez R L, Lacerda Santos A F and Rezende S M 2011 Spin pumping and anisotropic magnetoresistance voltages in magnetic bilayers: theory and experiment *Phys. Rev. B* **83** 144402
[18] Sagasta E, Omori Y, Isasa M, Gradhand M, Hueso L E, Niimi Y, Otani Y and Casanova F 2016 Tuning the spin Hall effect of Pt from the moderately dirty to the superclean regime *Phys. Rev. B* **94** 060412
[19] Vlaminck V, Pearson J E, Bader S D and Hoffmann A 2013 Dependence of spin-pumping spin Hall effect measurements on layer thicknesses and stacking order *Phys. Rev. B* **88** 064414
[20] Hung H Y, Luo G Y, Chiu Y C, Chang P, Lee W C, Lin J G, Lee S F, Hong M and Kwo J 2013 Detection of inverse spin Hall effect in epitaxial ferromagnetic Fe3Si films with normal metals Au and Pt *J. Appl. Phys.* **113** 17C507
[21] Isasa M, Villamor E, Hueso L E, Gradhand M and Casanova F 2015 Temperature dependence of spin diffusion length and spin Hall angle in Au and Pt *Phys. Rev. B* **91** 024402
[22] Kondou K, Sukegawa H, Mitani S, Tsukagoshi K and Kasai S 2012 Evaluation of spin Hall angle and spin diffusion length by using spin current-induced ferromagnetic resonance *Appl. Phys Express* **5** 073002
[23] Sangiao S, Morales-Aragonés J I, Lucas I, Jiménez-Cavero P, Morellón L, Sánchez-Azqueta C and De Teresa J M 2021 Optimization of YIG/Bi stacks for spin-to-charge conversion and influence of aging *J. Appl. Phys.* **54** 375305
[24] Fan J and Eom J 2008 Direct electrical observation of spin Hall effect in Bi film *Appl. Phys. Lett.* **92** 142101
[25] Isasa M *et al* 2016 Origin of inverse Rashba-Edelstein effect detected at the Cu/Bi interface using lateral spin valves *Phys. Rev. B* **93** 014420
[26] Papaioannou E, Fuhrmann P, Jungfleisch M B, Brächer T, Pirro P, Lauer V, Lösch J and Hillebrands B 2013 Optimizing the spin-pumping induced inverse spin Hall voltage by crystal growth in Fe/Pt bilayers *Appl. Phys. Lett.* **103** 162401
[27] Groen I *et al* 2023 Emergence of large spin-charge interconversion at an oxidized Cu/W interface *Phys. Rev. B* **107** 184438
[28] Pai C-F, Liu L, Li Y, Tseng H W, Ralph D C and Buhrman R A 2012 Spin transfer torque devices utilizing the giant spin Hall effect of tungsten *Appl. Phys. Lett.* **101** 122404
[29] Bansal R, Nirala G, Kumar A, Chaudhary S and Muduli P K 2018 Large spin Hall angle in β-W thin films grown on CoFeB without oxygen plasma *SPIN* **08** 1850018
[30] Tserkovnyak Y, Brataas A and Bauer G E W 2002 Spin pumping and magnetization dynamics in metallic multilayers *Phys. Rev. B* **66** 224403
[31] Hahn C, de Loubens G, Naletov V V, Ben Youssef J, Klein O and Viret M 2014 Conduction of spin currents through insulating antiferromagnetic oxides *EPL (Europhysics Letters)* **108** 57005
[32] Hao Q, Chen W and Xiao G 2015 Beta (β) tungsten thin films: structure, electron transport, and giant spin Hall effect *Appl. Phys. Lett.* **106** 182403
[33] Demasius K-U, Phung T, Zhang W, Hughes B P, Yang S-H, Kellock A, Han W, Pushp A and Parkin S S P 2016 Enhanced spin–orbit torques by oxygen incorporation in tungsten films *Nat. Commun.* **7** 10644
[34] Jhajhria D, Behera N, Pandya D K and Chaudhary S 2019 Dependence of spin pumping in W/CoFeB heterostructures on the structural phase of tungsten *Phys. Rev. B* **99** 014430
[35] Costa M, Costa A T and Hu J, Wu RQ and Muniz RB 2018 β-tungsten: a promising metal for spintronics *J. Phys.* **30** 305802
[36] Fan P, Yi K, Shao J-D and Fan Z-X 2004 Electrical transport in metallic films *J. Appl. Phys.* **95** 2527–31
[37] Reiss G, Brückl H and Vancea J 2001 Multilayers: electrical properties, Fuchs/Sondheimer model *Encyclopedia of Materials* (Science and Technology. Elsevier) pp 5876–82
[38] Stancil D D and Prabhakar A 2009 *Spin Waves—Theory and Applications* (Springer)
[39] Jungfleisch M B, Chumak A V, Kehlberger A, Lauer V, Kim D H, Onbasli M C, Ross C A, Kläui M and Hillebrands B 2015 Thickness and power dependence of the spin-pumping effect in Y3Fe5O12/Pt heterostructures measured by the inverse spin Hall effect *Phys. Rev. B* **91** 134407
[40] Haertinger M, Back C H, Lotze J, Weiler M, Geprägs S, Huebl H, Goennenwein S T B and Woltersdorf G 2015 Spin pumping in YIG/Pt bilayers as a function of layer thickness *Phys. Rev. B* **92** 054437
[41] d'Allivy Kelly O *et al* 2013 Inverse spin Hall effect in nanometer-thick yttrium iron garnet/Pt system *Appl. Phys. Lett.* **103** 082408
[42] Ruiz-Gómez S *et al* 2018 Highly Bi-doped Cu thin films with large spin-mixing conductance *APL Mater.* **6** 1011071–8
[43] Du C, Wang H, Yang F and Hammel P C 2014 Enhancement of pure spin currents in spin pumping Y3Fe5O12/Cu/metal trilayers through spin conductance matching *Phys. Rev. Appl.* **1** 044004
[44] Yang F and Chris Hammel P 2018 FMR-driven spin pumping in Y3Fe 5O 12-based structures *J. Phys. D: Appl. Phys.* **51** 253001
[45] Castel V, Vlietstra N, Ben Youssef J and van Wees B J 2012 Platinum thickness dependence of the inverse spin-Hall voltage from spin pumping in a hybrid yttrium iron garnet/platinum system *Appl. Phys. Lett.* **101** 1324041–44044
[46] Ando K *et al* 2011 Inverse spin-Hall effect induced by spin pumping in metallic system *J. Appl. Phys.* **109** 103913

[47] Hahn C, de Loubens G, Klein O, Viret M, Naletov V V and Ben Youssef J 2013 Comparative measurements of inverse spin Hall effects and magnetoresistance in YIG/Pt and YIG/Ta *Phys. Rev. B* **87** 174417

[48] Ando K, Yoshino T and Saitoh E 2009 Optimum condition for spin-current generation from magnetization precession in thin film systems *Appl. Phys. Lett.* **94** 1525091–3

[49] Gupta S, Medwal R, Kodama D, Kondou K, Otani Y and Fukuma Y 2017 Important role of magnetization precession angle measurement in inverse spin Hall effect induced by spin pumping *Appl. Phys. Lett.* **110** 0224041–5

[50] Nguyen M-H, Ralph D C and Buhrman R A 2016 Spin torque study of the spin Hall conductivity and spin diffusion length in platinum thin films with varying resistivity *Phys. Rev. Lett.* **116** 126601

[51] Elliott R J 1954 Theory of the effect of spin-orbit coupling on magnetic resonance in some semiconductors *Phys. Rev.* **96** 266–79

[52] Yafet Y 1963 *G Factors and Spin-Lattice Relaxation of Conduction Electrons* ed F Seitz and D Turnbull (Academic) pp 1–98

[53] Hao Q and Xiao G 2015 Giant spin Hall effect and switching induced by spin-transfer torque in W /Co40 Fe40 B20/MgO structure with perpendicular magnetic anisotropy *Phys. Rev. Appl.* **3** 034009

[54] Neumann L, Meier D, Schmalhorst J, Rott K, Reiss G and Meinert M 2016 Temperature dependence of the spin Hall angle and switching current in the nc-W(O)/CoFeB/MgO system with perpendicular magnetic anisotropy *Appl. Phys. Lett.* **109** 1424051–4

[55] Mazraati H, Chung S, Houshang A, Dvornik M, Piazza L, Qejvanaj F, Jiang S, Le T Q, Weissenrieder J and Åkerman J 2016 Low operational current spin Hall nano-oscillators based on NiFe/W bilayers *Appl. Phys. Lett.* **109** 242402

[56] Okuno T, Taniguchi T, Kim S, Baek S-H C, Park B-G, Moriyama T, Kim K-J and Ono T 2016 Temperature dependence of spin Hall magnetoresistance in W/CoFeB bilayer *Jpn. J. Appl. Phys.* **55** 080308

[57] Kim G W *et al* 2021 Spin–orbit torque engineering in β-W/CoFeB heterostructures with W–Ta or W–V alloy layers between β-W and CoFeB *NPG Asia Mater.* **13** 60–69

[58] Li Y, Zha X, Zhao Y, Lu Q, Li B, Li C, Zhou Z and Liu M 2022 Enhancing the spin–orbit torque efficiency by the insertion of a sub-nanometer β-W layer *ACS Nano* **16** 11852–61

[59] Sui X, Wang C, Kim J, Wang J, Rhim S H, Duan W and Kioussis N 2017 Giant enhancement of the intrinsic spin Hall conductivity in β-tungsten via substitutional doping *Phys. Rev. B* **96** 241105

[60] Cho S, Baek S-H C, Lee K-D, Jo Y and Park B-G 2015 Large spin Hall magnetoresistance and its correlation to the spin-orbit torque in W/CoFeB/MgO structures *Sci. Rep.* **5** 14668

[61] Kim J, Sheng P, Takahashi S, Mitani S and Hayashi M 2016 Spin Hall magnetoresistance in metallic bilayers *Phys. Rev. Lett.* **116** 097201

[62] Qiu Z, An T, Uchida K, Hou D, Shiomi Y, Fujikawa Y and Saitoh E 2013 Experimental investigation of spin Hall effect in indium tin oxide thin film *Appl. Phys. Lett.* **103** 182404

[63] Texas Instruments 2025 Texas instruments OP07 operational amplifier (available at: www.ti.com/product/OP07?keyMatch=OP07&tisearch=universal_search&usecase=GPN-ALT) (Accessed 22 September 2025)

[64] Wang H L, Du C H, Pu Y, Adur R, Hammel P C and Yang F Y 2013 Large spin pumping from epitaxial $Y_3Fe_5O_{12}$ thin films to Pt and W layers *Phys. Rev. B* **88** 100406

[65] Du C H, Wang H L, Pu Y, Meyer T L, Woodward P M, Yang F Y and Hammel P C 2013 Probing the spin pumping mechanism: exchange coupling with exponential decay in $Y_3Fe_5O_{12}$/Barrier/Pt heterostructures *Phys. Rev. Lett.* **111** 247202

[66] Wang H L, Du C H, Pu Y, Adur R, Hammel P and Yang F 2014 Scaling of spin Hall angle in 3d, 4d, and 5d metals from $Y_3Fe_5O_{12}$/metal spin pumping *Phys. Rev. Lett.* **112** 197201

[67] Obstbaum M, Härtinger M, Bauer H G, Meier T, Swientek F, Back C H and Woltersdorf G 2014 Inverse spin Hall effect in Ni81Fe19/normal-metal bilayers *Phys. Rev. B* **89** 060407

[68] Mosendz O, Pearson J E, Fradin F Y, Bauer G E W, Bader S D and Hoffmann A 2010 Quantifying spin Hall angles from spin pumping: experiments and theory *Phys. Rev. Lett.* **104** 046601